

Constant depth magic state cultivation with Clifford measurements by gauging

Bence Hetényi,^{1,*} Benjamin J. Brown,^{1,2} and Dominic J. Williamson^{3,†}

¹*IBM Quantum, IBM T. J. Watson Research Center, Yorktown Heights, New York*

²*IBM Denmark, Sundkrogsgade 11, 2100 Copenhagen, Denmark*

³*IBM Quantum, IBM Almaden Research Center, San Jose, CA 95120, USA*

(Dated: March 2026)

Magic states are a scarce resource for two-dimensional qubit stabilizer codes. Magic state cultivation was recently proposed to reduce the cost of magic state preparation by measuring the transversal Clifford operator of the color code. Cultivation achieves $\sim 10^{-9}$ logical error rates for the $d = 5$ color code, with substantially lower space-time overhead than magic state distillation. However, due to the $\mathcal{O}(d)$ depth of the Clifford measurement circuit, magic state cultivation becomes impractical for $d > 5$. Here, we perform logical XS^\dagger measurements on the color code by gauging a transversal Clifford gate, resulting in a constant-depth logical measurement circuit. We employ repeated gauging measurements with post-selection rather than performing error correction on the Clifford stabilizer code that emerges during the gauging protocol, thus gaining simplicity at the cost of scalability. Our protocol requires a regular square grid connectivity and yields logical error rates comparable to magic state cultivation. The $d = 7$ version of our protocol gives access to the 10^{-12} logical error rate regime at 0.05% physical error rate while retaining more than 1% of the shots after the equivalent of the cultivation stage.

I. INTRODUCTION

Magic states are an essential resource for fault-tolerant quantum computation because they complement Clifford operations to form a universal gate set. Preparing magic states fault-tolerantly using two-dimensional codes is challenging due to the Bravyi-König bound which restricts relevant local transversal gates to be Clifford [1]. Recent work has revealed new approaches to overcome this limitation in two dimensional codes [2–7], most approaches continue to rely on probabilistic preparation of magic states even in architectures with nonlocal connectivity [8, 9].

The most commonly used probabilistic approach is magic state distillation [10]. Distillation is most commonly implemented via a logical circuit that consumes a number of noisy magic states to produce fewer magic states that are less noisy. The distillation circuit is post-selected on undesirable measurement outcomes, and so succeeds only probabilistically. Many improvements have been made to reduce the cost of magic state distillation, however, there is still a considerable overhead required to prepare logical magic states in the surface code compared to other logical gates [10–12].

Measuring a transversal Clifford operator of a self-dual code [13–17] provides a simple alternative method to improve the fidelity of a non-stabilizer magic state, as opposed to distillation where the purification of the state requires multiple logical qubits and operations. A similar scheme that introduced several further optimizations, dubbed cultivation, was introduced in Ref. [18] where the logical XS^\dagger operator of the color code was measured using a circuit of

depth $\mathcal{O}(d)$ while respecting square grid connectivity. Cultivation achieved a logical error rate of $6 \cdot 10^{-10}$ in the $d = 5$ color code with a success probability of 15% at 0.1% physical error rate. A number of follow up works on Cultivation have appeared more recently [19–21].

Gauging provides an alternative approach to implementing a logical Clifford measurement with a low-depth adaptive quantum circuit [2, 22]. This is highly desirable, as it reduces the circuit depth of the Clifford measurement step to $\mathcal{O}(1)$. While the scheme of Ref. [22] is applicable to Clifford operators, constructing a suitable ancilla system that respects the geometric constraints presents a challenge.

Here, we provide a practical implementation of the gauging logical Clifford measurement protocol using a planar network of ancilla and flag qubits. Our scheme has the same hardware requirements as Ref. [18], but performs the Clifford measurement step in constant circuit depth. We show that the $d = 7$ version of our protocol can achieve logical error rates below $5 \cdot 10^{-12}$ for 0.05% physical error rate while retaining 1.5% of the shots after post selection.

II. GAUGING CLIFFORD MEASUREMENT

In this section, we briefly summarize the gauging logical measurement scheme introduced in Ref. [22] without assuming that the logical operator is a Pauli product, see App. B for further discussion. Consider a transversal logical operator of the form $C_L = \prod_i U_i$, where $U_i = U_i^{-1}$ and i runs over the data qubits. Note, $U_i = U_i^{-1}$ holds for all Hermitian Clifford operators, including those that are not Pauli. We define an ancilla system where each ancilla is connected to a pair of data qubits and is prepared in the $|0\rangle$ state at the beginning of the protocol. Gauss law

* bence.hetenyi@ibm.com

† Current address: School of Physics, University of Sydney, Sydney, NSW 2006, Australia

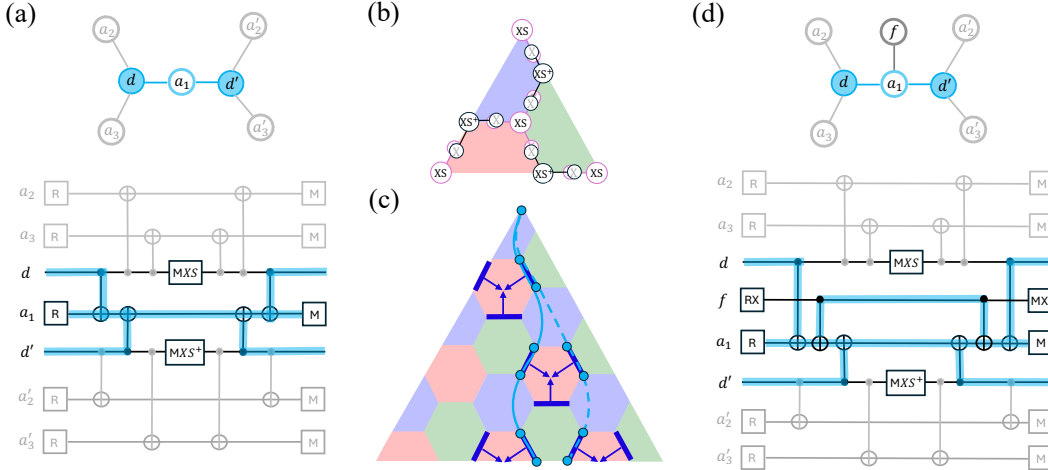


Figure 1. (a) Gauging measurement of the logical XS^\dagger operator supported on data qubits (d and d') using ancillas (a and a') on the edges of the honeycomb lattice. The weight of logical Z operator (cyan) is reduced during the measurement. (b) Gauge operators for measuring the transversal XS^\dagger on the $d = 3$ color code. (c) Two minimum-weight logical representatives (solid and dashed cyan lines) of the $d = 7$ color code. Arrows point at the flag qubit shared by the same colored edges. (d) Flagged version of the circuit in (a), where an extra qubit (f) increases the weight of the logical before the the circuit distance would drop.

operators are defined for every data qubit as follows

$$A_i = U_i \prod_{a \in \partial i} X_a. \quad (1)$$

The product of these operators is the logical operator C_L we aim to measure. In Ref. [22] it is shown that measuring these gauge operators satisfies (i) the product of measurements $\sigma_L = \prod_i m_i$ is the logical eigenvalue and (ii) the measurement outcome of the ancilla qubits is sufficient to restore the correct post-measurement state $(1 + \sigma_L C_L) |\psi\rangle_Q$ by applying the correction operator $\prod_{i \in Q'} U_i$ on a subset of data qubits $Q' \subset Q$ (see App. C for the proof).

We define the ancilla graph G by identifying data qubits with vertices and ancilla qubits with the edges of the graph. In that case the subset Q' of data qubits can be determined by taking an arbitrary edge path from an arbitrarily chosen qubit j to every other qubit $i \neq j$, and include i in the subset only if the parity of ancilla measurement outcomes along the edge path is odd.

In order to achieve fault tolerance and constant qubit overhead, it is sufficient for the ancilla graph G to fulfill the following properties (i) the length of the edge path between any pair of qubits included in a stabilizer should be constant, (ii) the Cheeger constant of the graph $h(G)$ should be sufficiently large, and (iii) the graph G should admit a sparse cycle basis [22].

In the case when U_i are Hermitian Clifford operators that are not Pauli, there is an additional criterion that needs to be fulfilled, independent of how the Clifford operator is measured. I.e., both cultivation and the gauging Clifford measurement need to respect this. In a self-dual CSS code, at least one type of stabilizers, X or Z , will not generally commute with the transversal Clifford operator.

Commutation is only achieved when the state is in the mutual $+1$ eigenspace of all the stabilizers of the other type. E.g., $H_{XY}X = XH_{XY}Z$, where $H_{XY} = \sqrt{i}XS^\dagger$ swaps X and Y and flips the sign of Z . In that case the X stabilizers only commute with the measurement of the logical XS^\dagger in the $+1$ eigenspace of the Z stabilizers.

II.1. Gauging logical Clifford measurement on the color code

We now consider the honeycomb color code with triangular boundary conditions [23], see App. A for a review. This code is self dual, and has weight-six (weight-four) X and Z plaquette stabilizers in the bulk (at the boundary). Logical Pauli, as well as Clifford operators are transversal (e.g., XS^\dagger). The plaquettes are three-colorable and we assign the color of the weight-four plaquette at each corner of the triangle to the respective corner and the edge opposite to it. Low-weight logical Pauli operators can be constructed by finding a Pauli string between a corner and the corresponding edge such that it goes through plaquettes of the same color (see Fig. 1(c)).

To measure the transversal logical XS^\dagger operator of the color code we use an ancilla system such that every pair of adjacent vertices on the honeycomb lattice is connected to the same ancilla qubit. This way, the data and ancilla qubits form a heavy hexagonal (heavy-hex) lattice (see Fig. 1(b) and App. B). The resulting ancilla graph G is connected, contains short loops [24] but has a Cheeger constant $h(G) < 1$. In this case the circuit distance of the protocol is reduced.

To clearly demonstrate where the bottleneck of the gauging logical measurement is, we show the path of a logi-

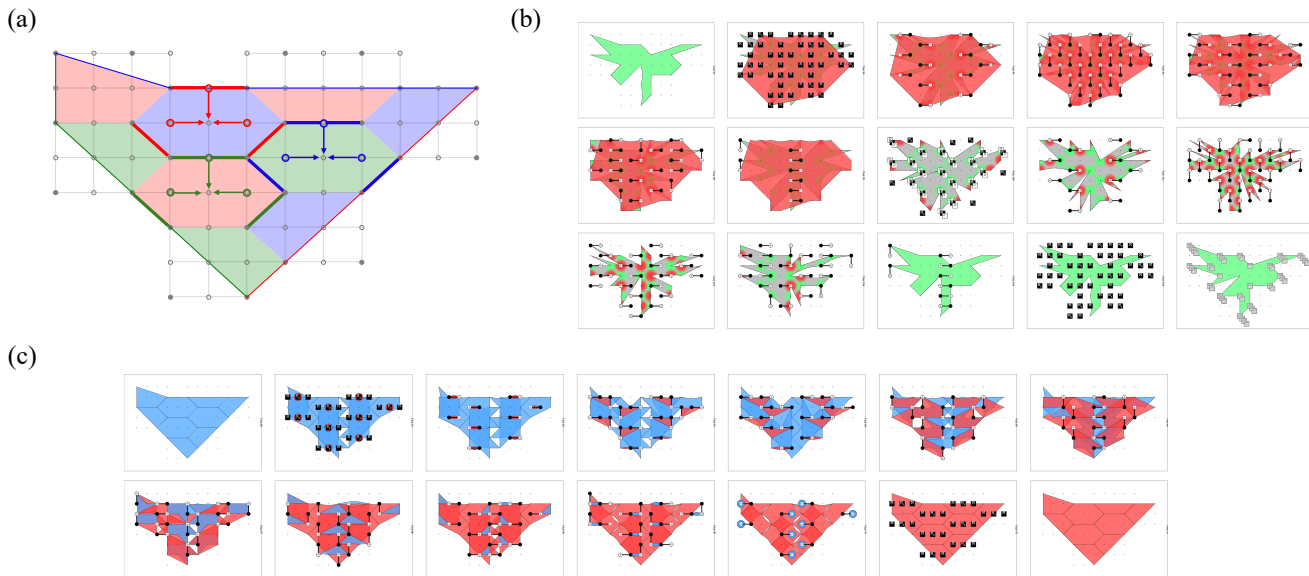


Figure 2. (a) Qubit layout for the square-grid implementation of the gauging Clifford measurement. In the middle of each plaquette there is a flag qubit, that flags the three edges that are parallel with one of the boundaries. The top left corner is deformed to reduce the number of extra qubits (needed for the ancilla cycles) at the boundary. (b) Circuit schedule of the a gauging logical (Y) measurement step. The two detector slices show a contracting (exists in steps 1 to 8) and an expanding logical Y check (steps 2 to 15). (c) Circuit schedule for one stabilizer measurement round. Detector slices correspond to the contracting Z (blue) and the expanding X detectors (red). Contracting X and expanding Z detectors are not shown on the figure for clarity.

cal Z operator during the protocol. While the logical Z does not have a deterministic eigenvalue, having a low-weight representative during the circuit can flip the prepared $|T\rangle = (|0\rangle + e^{i\pi/4}|1\rangle)/\sqrt{2}$ state. Fig. 1(a) shows how a ZZ operator on two data qubits is contracted to a single ancilla qubit during the measurement of the gauge operators. Since this weight-reduction happens along every edge of the lattice, the minimum-weight logical representatives shrink to $\lceil d/2 \rceil$ qubits, cf. the discussion of circuit distance in Ref. [22]. In the next section, we show how to avoid this distance-reduction using flag qubits and provide an efficient qubit layout where $(n-1)/2$ flag qubits are enough to flag all $\approx 3n/2$ edges in the honeycomb lattice.

III. GAUGING CLIFFORD MEASUREMENT WITH FLAG QUBITS

In order to avoid the weight reduction of a logical Z operator shown in Fig. 1(a), we employ a flag qubit f , adjacent to the ancilla a_1 , prepared in the $|+\rangle$ state. Applying a CX gate, controlled on the flag and targeted on the ancilla, before the step where the distance-reduction happens, the logical Z operator expands to the flag qubit. This way the fault distance is maintained throughout the protocol. This is shown in Fig. 1(d).

Next, we argue that one flag qubit per plaquette is sufficient to avoid the weight reduction of every minimum-weight logical Z representatives. As shown in Fig. 1(c), minimum-weight logicals that connect the blue corner to

the blue boundary of the color code are supported on edges that connect blue plaquettes. Furthermore, none of these representatives can contain two of such edges around the same plaquette. Otherwise the weight could be reduced by multiplying the logical with the corresponding stabilizer (hence the logical was not of minimum weight). Therefore, one may use the same flag qubit, to avoid the distance reduction along all three edges of a given plaquette. This leads to a factor of three reduction of flag qubit count.

From the point of view of the minimum-weight logical, flagging the edge parallel to the boundary is not necessary. However we find that omitting the boundary-parallel edges from the flagging for every color does reduce the fault distance, which is believed to be a consequence of the weight-reduction of higher-weight logicals. Therefore, in this work we included every edge in the flagging.

In order to find a suitable two-dimensional qubit layout for the flagged protocol, we need a lattice that (i) supports data qubits in a hexagonal sublattice, (ii) has one ancilla qubit in-between every nearest-neighbor pair of data qubits, and (iii) has one flag qubit per plaquette, connected to three ancilla qubits around it. Therefore, an elementary unit cell of a regular lattice that can accommodate the flagged gauging measurement protocol needs to contain two data, three ancilla and one flag qubits. Disregarding the boundary, this is 50% higher qubit count than required for cultivation.

The embedding of this lattice in a regular square grid is shown in Fig. 2(a). There are additional data qubits and ancillas around the boundary of the lattice. These ensure

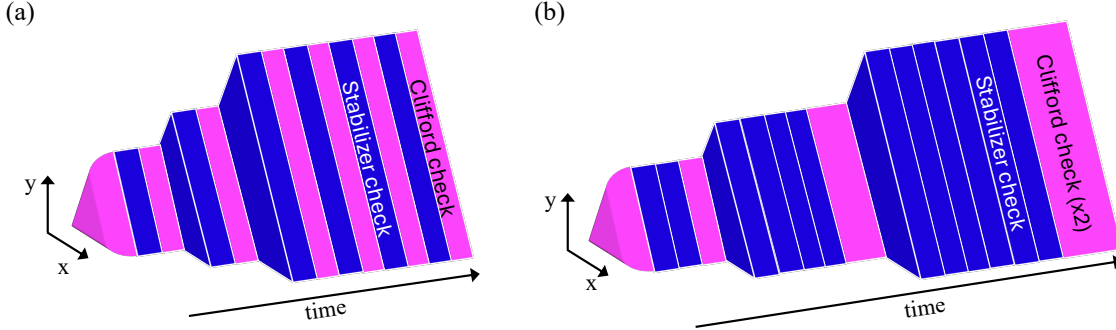


Figure 3. (a) Gauging Clifford measurements on a growing the lattice (intermediate code distances $d_{\text{int}} \in \{3, 5, 7\}$). Starting with a unitary injection, one stabilizer measurement and one Clifford check is performed at every stage until the target distance, where the remaining $(d+1)/2$ rounds take place. (b) Cultivation in the strictly distance-preserving scheme with $d-1$ stabilizer rounds before every Clifford double check. Blue slices denote stabilizer measurements and imply growing with physical Bell-state preparations unless preceded with a Clifford check of the same distance.

that there are complete cycles in the ancilla graph even at the boundary plaquettes (as required for the ancilla system in the third condition of the gauging protocol). Such cycles introduce a redundancy that is necessary to identify measurement errors on the ancillas [22]. The additional data qubits are always initialized in the appropriate basis before the gauging measurement and therefore do not influence the measured eigenvalue.

Having all the necessary components for the gauging logical measurement in the coupling graph, we turn to the syndrome measurement circuit of the color code. To this end we use the superdense syndrome measurement circuit of Ref. [25] and prepare the ancilla Bell pair on the two ancillas that are inside each plaquette. This can be done by initializing the ancillas and the flag qubit and applying three CX gates, i.e., $CX_{a_2,f}CX_{f,a_2}CX_{f,a_1}|0\rangle_{a_1}|+\rangle_f|0\rangle_{a_2}$. Since every data qubit on a given plaquette is the nearest neighbor of either a_1 or a_2 , we can follow Ref. [25] to encode the X and Z plaquette information into the Bell state of the ancillas. We alternate the role of the ancillas between neighboring columns of hexagons, and shift the superdense CX schedule by two time steps between the left and right sides of each plaquette. The measurement of the Bell state is performed reversing the role of the ancillas. This allows us to shorten the circuit depth by one (10 CX layers instead of 12). See Fig. 2(c) for the contracting Z-type (expanding X-type) detecting regions.

The CX scheduling of the gauging measurement step is based on the following logic. Here we describe the schedule from the perspective of the three ancillas that belong to a plaquette, instead of the measurement of a single gauge operator. After resetting every ancilla and the flags we perform five CX layers. In the first one a CX is targeted on one of the three ancillas; in the second, the first edge-ancilla is flagged and another one is targeted from a data qubit; in the third step the first edge is finished, the second is being flagged and the third one is targeted from a data qubit; the fourth step finishes the second edge, flags the

third, before the third edge would be finished in the last step. We then proceed by measuring the data qubits. Afterwards, the CX layers are repeated, which completes the gauge measurements, and the ancillas are measured along with the flags. Finally, based on the ancilla outcomes, we restore the codespace using physical Clifford operations. See Fig. 2(b) where the contracting detector compares the logical Y measurement of this round with that of the previous round, and the expanding detector compares this measurement with the next one.

There are opportunities for pipelining the circuit described above if two-qubit gates can be applied during measurements on disjoint subsets of qubits. This allows us to reduce the circuit depth of one syndrome and one Clifford measurement to 18 CX and 5 measurement (reset) layers (see Fig. 5 for details). For context, cultivation achieves an equivalent task in $\frac{3}{2}(d+5)$ CX and 4 measurement (reset) layers.

To prepare magic states of larger fault distance d_f we start from the $d=3$ example and prepare magic state non fault-tolerantly using a unitary circuit. This is followed by a stabilizer measurement and a gauging Clifford check at $d_{\text{int}}=3$. We grow the lattice by preparing Bell states on the edges that match the color of the boundary we are growing along. We continue this until we reach the final target distance, where we perform an additional $(d+1)/2$ rounds of stabilizer and Clifford check pairs. See Fig. 3(a) for a process diagram of the growing stages. The reason we cannot do two Clifford checks at every intermediate distance is the existence of spacetime-diagonal errors, that start at the previous spatial boundary and terminate at the opposite corner of the final code in last time step. Such an error flips the logical state at the last growing step, and mutes every logical detector along the way. Such errors are the consequence of the growing step, and have nothing to do with the gauging measurement scheme. In fact, these type of errors are the reason why cultivation requires $d-1$ stabilizer rounds before the Clifford double-check at every

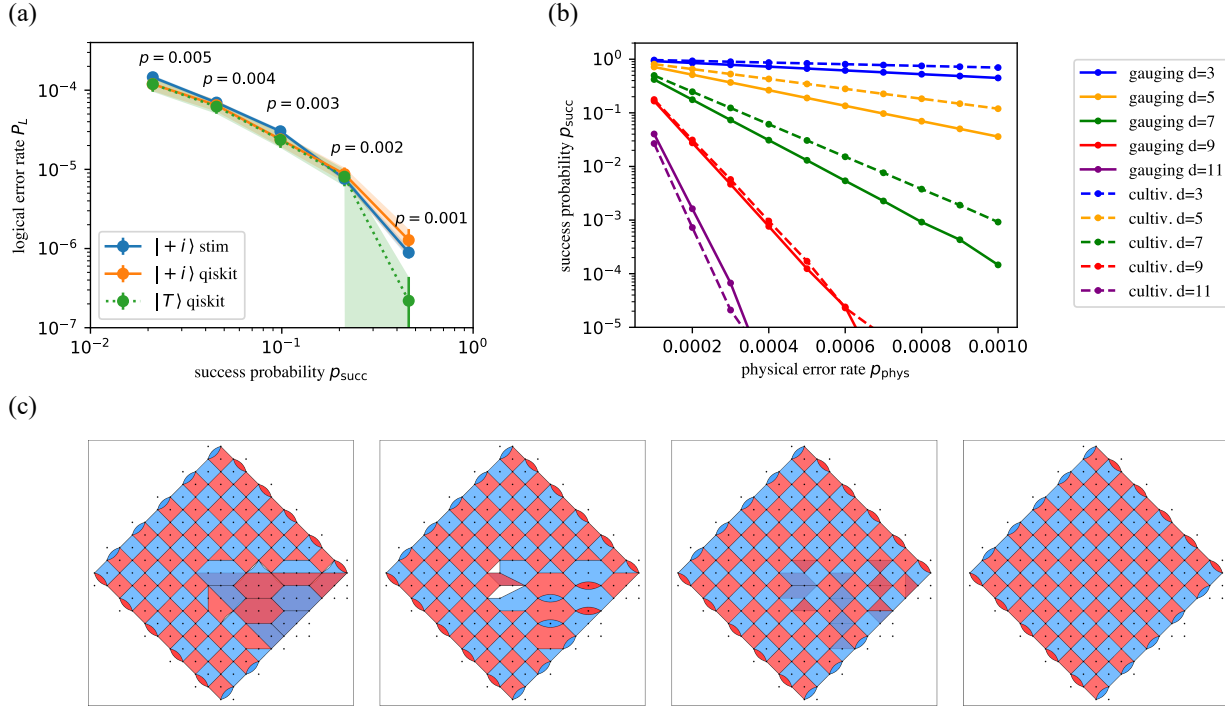


Figure 4. (a) Comparison of different simulation methods for the $d = 3$ gauging logical measurement protocol under uniform circuit-level noise for various physical error rates p . The Clifford simulations of the $|+i\rangle$ state preparation, obtained via `stim`, align with that of the statevector simulation and the $|T\rangle$ -state preparation. (b) Comparison between the gauging Clifford measurement and magic state cultivation for uniform circuit-level noise. For this noise model the break-even point in success probability is $d = 9$. (c) Transitioning to a regular surface code patch in three rounds. The first round involves a reset, six CX, and a measurement layer; the second is similar with three CX rounds; the last one is a regular surface code syndrome cycle. See Fig. 6 for the full circuit.

intermediate distance (see Fig. 3(b))[18].

IV. SIMULATIONS AND COMPARISON WITH CULTIVATION

In order to verify that the gauging Clifford measurement scheme prepares the desired state, we performed full statevector simulations using `qiskit` on the $d = 3$ example (25 qubits in total) [26]. The simulated protocol consists of a unitary $|T\rangle$ -state preparation and two rounds of stabilizer and Clifford checks for uniform circuit level noise with physical error rates between 0.1% and 0.5% (see Fig. 4(a)). The uniform circuit-level noise model considered here is equivalent to that of Ref. [18] and we used the pipelined circuit in the simulation. We observe good agreement between the statevector simulations and the $|+i\rangle$ version simulated with `stim` [27]. In both cases, the logical error probability is obtained by Monte-Carlo sampling and full post-selection. For the `qiskit` simulations we project the final state onto a stabilizer state and evaluate the expectation value of the $(X + Y)/\sqrt{2}$ operator on a shot-by-shot basis, while for the `stim` simulations we perform a noiseless stabilizer and final logical measurement in the Y basis. In both cases, the post selection on the final perfect round is

included in the success probability.

In Tab. I we show the relevant figures of merit at higher fault distances. While the success probability is somewhat lower than that of cultivation, the logical error rates are comparable for $d_f \in \{3, 5\}$ [18]. We also benchmark our protocol for $d = 7$ at $p_{\text{phys}} = 0.05\%$ and find an acceptable success probability for preparing a logical magic state with $\sim 10^{-12}$ logical error rate. We note that a comparison for higher distances and lower error rates would be highly interesting due to the asymptotic advantage of the gauging

p_{phys}	d_f	P_L	p_{succ}
0.1%	3	$(8.8 \pm 0.8) \times 10^{-7}$	46%
	5	$(3.2 \pm 0.4) \times 10^{-10}$	4%
	7	—	0.01%
0.05%	3	$(1.2 \pm 0.2) \times 10^{-7}$	65%
	5	$(1.1 \pm 0.3) \times 10^{-11}$	20%
	7	$< 5 \times 10^{-12}$	1.5%

Table I. Logical error probability P_L and success rate p_{succ} of the $|+i\rangle$ state preparation for different fault-distances d_f and physical error rates p_{phys} . For $d_f = 7$ at $p_{\text{phys}} = 0.1\%$ we did not perform Monte-Carlo sampling due to the small success rates, and for $p_{\text{phys}} = 0.05\%$ we did not observe any logical failure in $2 \cdot 10^{11}$ post-selected samples.

	Cultivation	This work
single Clifford check time	$(3d_{\text{int}} - 1)/2 t_{\text{CX}} + 2 t_{\text{M/R}}$	$8 t_{\text{CX}} + 3 t_{\text{M/R}}$
stabilizer time	$8 t_{\text{CX}} + 2 t_{\text{M/R}}$	$10 t_{\text{CX}} + 2 t_{\text{M/R}}$
# stabilizer rounds	$(d^2 - 1)/4$	$d-1$
total time / $(d - 1)$	$(11d + 15)/4 t_{\text{CX}} + (d + 5)/2 t_{\text{M/R}}$	$18 t_{\text{CX}} + 5 t_{\text{M/R}}$

Table II. Comparison of the circuit depth between cultivation and the gauging Clifford measurement protocol. The comparison assumes a final color code path of distance d and the patch is gradually grown achieving $d_f = d$. In the table, $3 \leq d_{\text{int}} \leq d$ is the code distance of the color code patch in the intermediate stage, $t_{\text{M/R}}$ is the measurement and reset duration, and t_{CX} is the duration of the CX gates. The number of Clifford checks is $d - 1$ in both cases, but cultivation requires $d_{\text{int}} - 1$ rounds after every growing step, and performs a double-check at every intermediate distance as shown in Fig 3.

Clifford measurement scheme in circuit depth. Unfortunately, we found no record of the performance on cultivation above $d = 5$. Furthermore, the fault-distance of the cultivation scheme with a $d = 5$ color code in Ref. [18] is only $d_f = 4$. While weight-4 errors do not limit the performance of the protocol at $p_{\text{phys}} = 0.1\%$ due to the low multiplicity of such errors, at lower error rates the $d_f = 5$ gauging protocol is expected to have an advantage.

In order to determine the break-even point in success probability between the gauging Clifford measurement and cultivation, we summarize the time overhead of both protocols in Tab. II. Note that in the table the time overhead of the Clifford check in the cultivation scheme is divided by two to account for the fact that the Clifford check circuit increases the time distance by two. This is in fact the biggest practical advantage of cultivation over the gauging measurement scheme. The gauging Clifford measurement scheme, on the other hand, brings two important improvements (*i*) the Clifford check has a constant-depth circuit (*ii*) the protocol requires $d - 1$ stabilizer and Clifford check rounds in total as opposed to cultivation, where each growing step requires $d - 1$ stabilizer rounds (see Fig. 3(b) for illustration). Taking stock, the break-even point in total circuit depth should be $d = 5$, however, this is not the most relevant figure of merit from a practical standpoint.

Fig. 4(b) shows the success probability of the gauging Clifford measurement vs. cultivation employing the respective growing strategies from Fig. 3. Under the uniform circuit-level noise model used in both works, the breakeven point in success probability only comes as $d = 9$. This is due to the qubit overhead of the gauging protocol. The latter uses 50% more qubits, resulting in similar number of fault locations only at $d = 9$ [28]. We note that the most important metric would be the success probability at a given logical error rate, but Monte-Carlo sampling for the logical error rate becomes unfeasible already at $d = 7$.

V. DISCUSSION

In this work we described a method to prepare logical magic states on a square grid by implementing post-selected Clifford measurement via gauging. Our scheme has the advantage of maintaining a constant circuit depth for the Clifford measurement. There are some additional advantages compared to the cultivation, by dividing the

lattice into two sublattices in a checkerboard-like pattern, data and flag qubits are occupying the same sublattice and ancillas are hosted on the other one. This separation reduces cross-talk between data qubits and has further advantages in architectures where data and ancilla qubits are distinguished at a physical level [29].

Furthermore, in the growing stage [18] it is possible to deform the color code portion into a regular surface code patch, as shown in Fig. 4(c). This opportunity arises from the commensurability of our color code lattice with the surface code. Including the flag qubits (third step on Fig. 4(c)) in the deformed color code allows one to keep most of the original detectors in the color code region. The regular surface code patch has a shallower syndrome measurement circuit and hence potentially better performance than the matchable grafted code of Ref. [18]. Rigorously assessing the usefulness of this approach requires end-to-end resource estimates.

Although direct comparison of the probability of success did not produce a clear advantage for $d = 7$, we note that there are further opportunities for optimization both in the circuit depth and the count of qubits. The space time overhead of the protocol could be optimized using a time-dynamic approach instead of designating the roles of data, ancilla, and flag to different qubits [30, 31].

Our work points to an interesting future direction of numerically and experimentally benchmarking a scalable error-corrected protocol for magic state preparation via gauging Clifford measurement. This requires the error-correction with a Clifford stabilizer code and a just-in-time decoder as explained in Ref. [2]. While initial results on implementing the measurement of relevant Clifford stabilizers on a planar geometry are presented in Appendix A, further work to improve the fault-tolerance of these circuits would be advantageous. Finally, it would be interesting to understand the performance landscape of protocols that interpolate between postselected error detection and full error correction for the preparation of magic states via logical Clifford measurement at a target error rate and footprint.

ACKNOWLEDGEMENTS

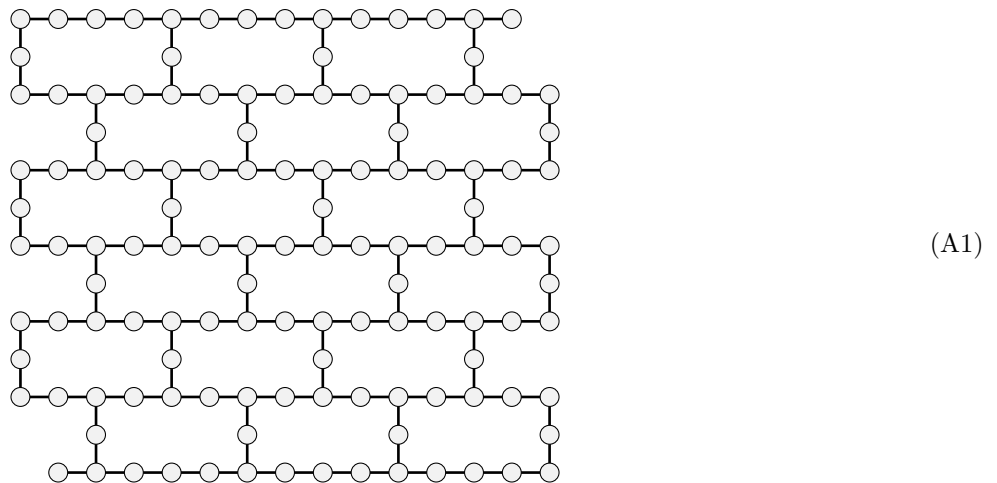
We thank Tomas Jochym-O'Connor for insightful discussions.

- [1] S. Bravyi and R. König, Classification of Topologically Protected Gates for Local Stabilizer Codes, *Physical Review Letters* **110**, 170503 (2013).
- [2] M. Davydova, A. Bauer, J. C. M. de la Fuente, M. Webster, D. J. Williamson, and B. J. Brown, Universal fault tolerant quantum computation in 2d without getting tied in knots, arXiv: 2503.15751 (2025).
- [3] A. Bauer and J. C. M. de la Fuente, *Planar fault-tolerant circuits for non-Clifford gates on the 2D color code* (2025), version Number: 1.
- [4] S.-J. Huang and Y. Chen, *Generating logical magic states with the aid of non-abelian topological order* (2025), arXiv:2502.00998 [quant-ph].
- [5] R. Kobayashi, G. Zhu, and P.-S. Hsin, *Clifford hierarchy stabilizer codes: Transversal non-clifford gates and magic* (2025), arXiv:2511.02900 [quant-ph].
- [6] S.-J. Huang, A. Warman, S. Schafer-Nameki, and Y. Chen, *Hybrid lattice surgery: Non-clifford gates via non-abelian surface codes* (2026), arXiv:2510.20890 [quant-ph].
- [7] A. Warman and S. Schafer-Nameki, *Transversal clifford-hierarchy gates via non-abelian surface codes* (2026), arXiv:2512.13777 [quant-ph].
- [8] T. J. Yoder, E. Schoute, P. Rall, E. Pritchett, J. M. Gambetta, A. W. Cross, M. Carroll, and M. E. Beverland, *Tour de gross: A modular quantum computer based on bivariate bicycle codes* (2025), arXiv:2506.03094 [quant-ph].
- [9] P. Webster, L. Berent, O. Chandra, E. T. Hockings, N. Baspin, F. Thomsen, S. C. Smith, and L. Z. Cohen, *The pinnacle architecture: Reducing the cost of breaking rsa-2048 to 100 000 physical qubits using quantum ldpc codes* (2026), arXiv:2602.11457 [quant-ph].
- [10] S. Bravyi and A. Kitaev, Universal quantum computation with ideal Clifford gates and noisy ancillas, *Physical Review A* **71**, 022316 (2005).
- [11] A. G. Fowler, M. Mariantoni, J. M. Martinis, and A. N. Cleland, Surface codes: Towards practical large-scale quantum computation, *Physical Review A* **86**, 032324 (2012).
- [12] D. Litinski, Magic State Distillation: Not as Costly as You Think, *Quantum* **3**, 205 (2019).
- [13] H. Goto, Minimizing resource overheads for fault-tolerant preparation of encoded states of the steane code, *Scientific Reports* **2016** 6:1 **6**, 19578 (2016).
- [14] C. Chamberland and A. W. Cross, Fault-tolerant magic state preparation with flag qubits, *Quantum* **3**, 143 (2019).
- [15] C. Chamberland and K. Noh, Very low overhead fault-tolerant magic state preparation using redundant ancilla encoding and flag qubits, *npj Quantum Information* **6**, 10.1038/s41534-020-00319-5 (2020).
- [16] R. S. Gupta, N. Sundaresan, T. Alexander, C. J. Wood, S. T. Merkel, M. B. Healy, M. Hillenbrand, T. Jochym-O'Connor, J. R. Wootton, T. J. Yoder, A. W. Cross, M. Takita, and B. J. Brown, Encoding a magic state with beyond break-even fidelity, *Nature* **625**, 259 (2024).
- [17] T. Itogawa, Y. Takada, Y. Hirano, and K. Fujii, Efficient magic state distillation by zero-level distillation, *PRX Quantum* **6**, 10.1103/thxx-njr6 (2025).
- [18] C. Gidney, N. Shutty, and C. Jones, *Magic state cultivation: Growing T states as cheap as CNOT gates* (2024), arXiv:2409.17595 [quant-ph].
- [19] Y. Vakinin, S. Jacoby, A. Grimsmo, and A. Retzker, *Efficient magic state cultivation on the surface code* (2026), arXiv:2502.01743 [quant-ph].
- [20] Z.-H. Chen, M.-C. Chen, C.-Y. Lu, and J.-W. Pan, *Efficient magic state cultivation on \mathbb{RP}^2* (2025), arXiv:2503.18657 [quant-ph].
- [21] K. Sahay, P.-K. Tsai, K. Chang, Q. Su, T. B. Smith, S. Singh, and S. Puri, *Fold-transversal surface code cultivation* (2025), arXiv:2509.05212 [quant-ph].
- [22] D. J. Williamson and T. J. Yoder, *Low-overhead fault-tolerant quantum computation by gauging logical operators* (2024), arXiv:2410.02213 [quant-ph].
- [23] H. Bombin and M. A. Martin-Delgado, Topological quantum distillation, *Physical Review Letters* **97**, 10.1103/PhysRevLett.97.180501 (2006), arXiv:0605138 [quant-ph].
- [24] At the boundary of the lattice one needs to extend the 4-body plaquettes with 2 data qubits in a known state to complete the cycles while preserving the connectivity.
- [25] C. Gidney and C. Jones, *New circuits and an open source decoder for the color code* (2023), arXiv:2312.08813 [quant-ph].
- [26] G. Aleksandrowicz, T. Alexander, P. Barkoutsos, L. Bello, Y. Ben-Haim, D. Bucher, F. J. Cabrera-Hernández, J. Carballo-Franquis, A. Chen, C.-F. Chen, J. M. Chow, A. D. Corcoles-Gonzales, A. J. Cross, A. Cross, J. Cruz-Benito, C. Culver, S. De La Puente González, E. De La Torre, D. Ding, E. Dumitrescu, I. Duran, P. Eendebak, M. Everitt, I. Faro Sertage, A. Frisch, A. Fuhrer, J. Gambetta, B. Godoy Gago, J. Gomez-Mosquera, D. Greenberg, I. Hamamura, V. Havlicek, J. Hellmers, L. Herok, H. Horii, S. Hu, T. Imamichi, T. Itoko, A. Javadi-Abhari, N. Kanazawa, A. Karazeev, K. Krsulich, P. Liu, Y. Luh, Y. Maeng, M. Marques, F. J. Martín-Fernández, D. T. McClure, D. McKay, S. Meesala, A. Mezzacapo, N. Moll, D. Moreda Rodriguez, G. Nannicini, P. Nation, P. Ollitrault, L. J. O'Riordan, H. Paik, J. Pérez, A. Phan, M. Pistoia, V. Prutyaynov, M. Reuter, J. Rice, A. Rodríguez Davila, R. H. Putra Rudy, M. Ryu, N. Sathaye, C. Schnabel, E. Schoute, K. Setia, Y. Shi, A. Silva, Y. Siraichi, S. Sivarajah, J. A. Smolin, M. Soeken, H. Takahashi, I. Tavernelli, C. Taylor, P. Taylour, K. Trubing, M. Treinish, W. Turner, D. Vogt-Lee, C. Vuillot, J. A. Wildstrom, J. Wilson, E. Winston, C. Wood, S. Wood, S. Worner, I. Yunus Akhalwaya, and C. Zoufal, Qiskit: An Open-source Framework for Quantum Computing, Zenodo 10.5281/zenodo.2562111 (2019).
- [27] C. Gidney, Stim: a fast stabilizer circuit simulator, *Quantum* **5**, 497 (2021), arXiv:2103.02202 [quant-ph].
- [28] For this rough estimate, we assume that the success rate depends the same way on the number of fault locations in both cases, and the number of fault locations is the total number of qubits times the total time. Further, we take $t_{CX} = t_{M/R}$ which describes well the uniform noise model.
- [29] N. Lacroix, A. Bourassa, F. J. H. Heras, L. M. Zhang, J. Bausch, A. W. Senior, T. Edlich, N. Shutty, V. Sivak, A. Bengtsson, M. McEwen, O. Higgott, D. Kafri, J. Claes, A. Morvan, Z. Chen, A. Zalcman, S. Madhuk, R. Acharya, L. A. Beni, G. Aigeldinger, R. Alcaraz, T. I. Andersen, M. Ansmann, F. Arute, K. Arya, A. Asfaw, J. Atalaya, R. Babbush, B. Ballard, J. C. Bardin, A. Bilmes, S. Blackwell, J. Bovard, D. Bowers, L. Brill, M. Broughton, D. A. Browne, B. Buchea, B. B. Buckley, T. Burger, B. Bur-

- kett, N. Bushnell, A. Cabrera, J. Campero, H.-S. Chang, B. Chiaro, L.-Y. Chih, A. Y. Cleland, J. Cogan, R. Collins, P. Conner, W. Courtney, A. L. Crook, B. Curtin, S. Das, S. Demura, L. D. Lorenzo, A. D. Paolo, P. Donohoe, I. Drozdov, A. Dunsworth, A. Eickbusch, A. M. Elbag, M. Elzouka, C. Erickson, V. S. Ferreira, L. F. Burgos, E. Forati, A. G. Fowler, B. Foxen, S. Ganjam, G. Garcia, R. Gasca, É. Genois, W. Giang, D. Gilboa, R. Gosula, A. G. Dau, D. Graumann, A. Greene, J. A. Gross, T. Ha, S. Habegger, M. Hansen, M. P. Harrigan, S. D. Harrington, S. Heslin, P. Heu, R. Hiltermann, J. Hilton, S. Hong, H.-Y. Huang, A. Huff, W. J. Huggins, E. Jeffrey, Z. Jiang, X. Jin, C. Joshi, P. Juhas, A. Kabel, H. Kang, A. H. Karamlou, K. Kechedzhi, T. Khaire, T. Khattar, M. Khezri, S. Kim, P. V. Klimov, B. Kobrin, A. N. Korotkov, F. Kostritsa, J. M. Kreikebaum, V. D. Kurilovich, D. Landhuis, T. Lange-Dei, B. W. Langley, P. Laptev, K.-M. Lau, J. Ledford, K. Lee, B. J. Lester, L. L. Guevel, W. Y. Li, Y. Li, A. T. Lill, W. P. Livingston, A. Locharla, E. Lucero, D. Lundahl, A. Lunt, A. Maloney, S. Mandrà, L. S. Martin, O. Martin, C. Maxfield, J. R. McClean, S. Meeks, A. Megrant, K. C. Miao, R. Molavi, S. Molina, S. Montazeri, R. Movasagh, C. Neill, M. Newman, A. Nguyen, M. Nguyen, C.-H. Ni, M. Y. Niu, L. Oas, W. D. Oliver, R. Orosco, K. Ottosson, A. Pizzuto, R. Potter, O. Pritchard, C. Quintana, G. Ramachandran, M. J. Reagor, R. Resnick, D. M. Rhodes, G. Roberts, E. Rosenberg, E. Rosenfeld, E. Rossi, P. Roushan, K. Sankaragomathi, H. F. Schurkus, M. J. Shearn, A. Shorter, V. Shvarts, S. Small, W. C. Smith, S. Springer, G. Sterling, J. Suchard, A. Szasz, A. Sztejn, D. Thor, E. Tomita, A. Torres, M. M. Torunbalci, A. Vaishnav, J. Vargas, S. Vdovichev, G. Vidal, C. V. Heidweiller, S. Waltman, J. Waltz, S. X. Wang, B. Ware, T. Weidel, T. White, K. Wong, B. W. K. Woo, M. Woodson, C. Xing, Z. J. Yao, P. Yeh, B. Ying, J. Yoo, N. Yosri, G. Young, Y. Zhang, N. Zhu, N. Zobrist, H. Neven, P. Kohli, A. Davies, S. Boixo, J. Kelly, C. Jones, C. Gidney, and K. J. Satzinger, [Scaling and logic in the color code on a superconducting quantum processor](#) (2024), [arXiv:2412.14256 \[quant-ph\]](#).
- [30] M. McEwen, D. Bacon, and C. Gidney, Relaxing Hardware Requirements for Surface Code Circuits using Time-dynamics, [Quantum](#) **7**, 1172 (2023).
- [31] M. H. Shaw and B. M. Terhal, Lowering Connectivity Requirements for Bivariate Bicycle Codes Using Morphing Circuits, [Physical Review Letters](#) **134**, 090602 (2025).
- [32] D. J. Williamson and B. Hetényi, [Dynamical quantum codes and logic gates on a lattice with sparse connectivity](#) (2025), [arXiv:2510.05225 \[quant-ph\]](#).
- [33] A. Prem and D. Williamson, Gauging permutation symmetries as a route to non-Abelian fractons, [SciPost Physics](#) **7**, 068 (2019), [arXiv:1905.06309](#).
- [34] B. Yoshida, Topological phases with generalized global symmetries, [Physical Review B](#) **93**, 155131 (2016), [arXiv:1508.03468](#).
- [35] M. Iqbal, N. Tantivasadakarn, R. Verresen, S. L. Campbell, J. M. Dreiling, C. Figgatt, J. P. Gaebler, J. Johansen, M. Mills, S. A. Moses, J. M. Pino, A. Ransford, M. Rowe, P. Siegfried, R. P. Stutz, M. Foss-Feig, A. Vishwanath, and H. Dreyer, Non-Abelian Topological Order and Anyons on a Trapped-Ion Processor, [Nature](#) **626**, 505 (2023), [arXiv:2305.03766v2](#).
- [36] M. Barkeshli, P. Bonderson, M. Cheng, and Z. Wang, Symmetry fractionalization, defects, and gauging of topological phases, [Physical Review B](#) **100**, 10.1103/PhysRevB.100.115147 (2019), [arXiv:1410.4540](#).
- [37] B. Hetényi and J. R. Wootton, Creating entangled logical qubits in the heavy-hex lattice with topological codes, [PRX Quantum](#) **5**, 040334 (2024).
- [38] H. Bombin, [2d quantum computation with 3d topological codes](#) (2018), [arXiv:1810.09571 \[quant-ph\]](#).
- [39] H. Bombin, Transversal gates and error propagation in 3D topological codes, [arXiv preprint](#) (2018), [arXiv:1810.09575](#).
- [40] B. J. Brown, A fault-tolerant non-clifford gate for the surface code in two dimensions, [Science Advances](#) **6**, 10.1126/SCIADV.AAY4929 (2020), [arXiv:1903.11634](#).

Appendix A: Color Code on the heavy-hex lattice

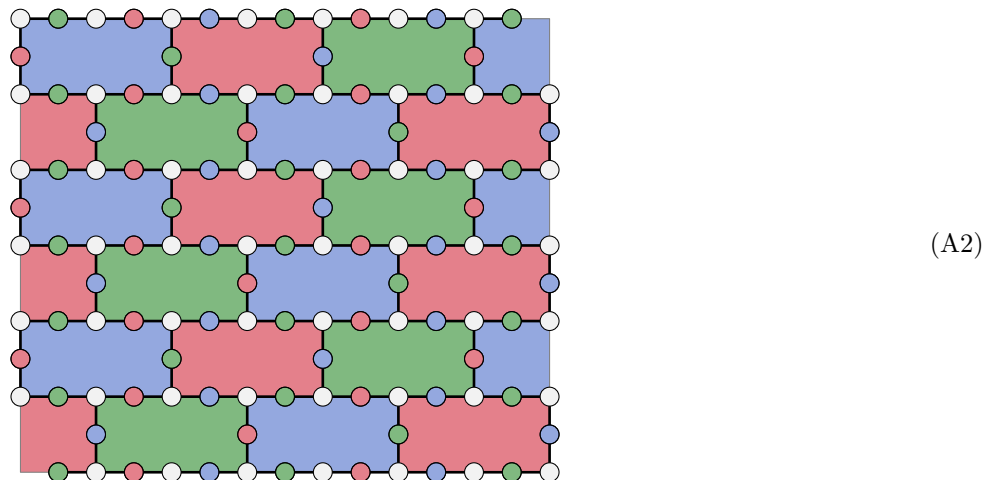
In this appendix, we review the Color Code and the heavy-hex lattice. Below we depict a patch of the heavy-hex lattice.



(A1)

The vertex-edge lattice structure of this qubit layout is well suited to implement a gauging logical measurement of a transversal logical operator.

It is convenient to introduce a 3-coloring of the plaquettes on the heavy-hex lattice when discussing the Color Code. This induces a 3-coloring of the edges on the heavy-hex lattice, shown below.



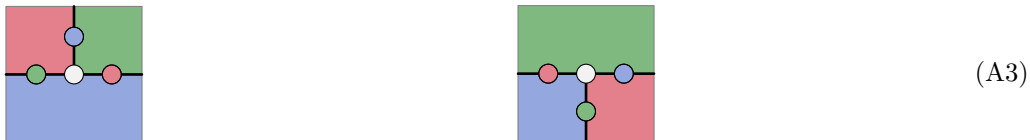
(A2)

The plaquette stabilizers of the Color Code can be measured on the heavy-hex lattice in a variety of ways, including via the procedure proposed in Ref. [32].

1. Square patch

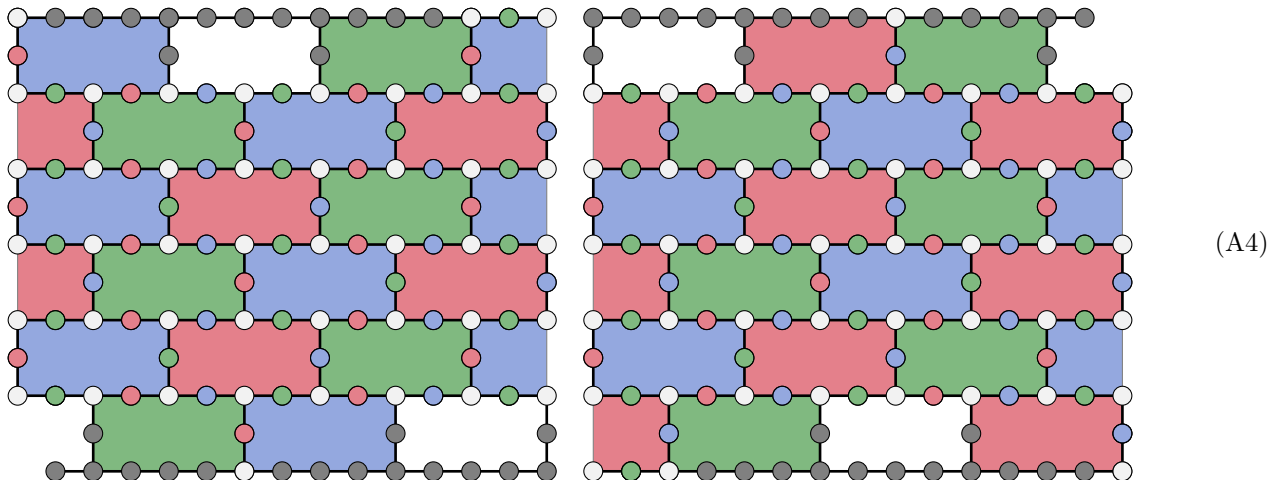
We first discuss a square patch of the Color Code with green vertical, and red or blue horizontal, boundary conditions. With these boundary conditions, the Color Code encodes a pair of logical qubits that support a transversal Hadamard gate that implements a logical Hadamard+SWAP transformation. This Color Code also supports a logical CZ gate that is implemented by a transversal gate given by a product of $\sqrt{-i}XS$ on *up* vertices, depicted on the left below, and $\sqrt{i}XS^\dagger$ on *down* vertices, depicted on the right below. For the remainder of this section we do not explicitly write the complex phase in front of $\sqrt{-i}XS$ and $\sqrt{i}XS^\dagger$, rather we write XS and XS^\dagger for notational simplicity, where the complex phases

required to make these operators are left implicit.



There are three possible color configurations for the up vertices, we have depicted a single choice for simplicity, and similarly for the down vertices. The product of XS and XS^\dagger gates described above preserves the code space, as $(XS)X(XS)^\dagger = Y$, and $(XS^\dagger)X(XS^\dagger)^\dagger = -Y$. This transversal action maps the X -type plaquette operators to Y -type plaquette operators with the appropriate (± 1) sign, determined by the parity of half the number of vertices in the plaquette. Similarly, the logical action depends on the length of the logical representative up to a (± 1) sign.

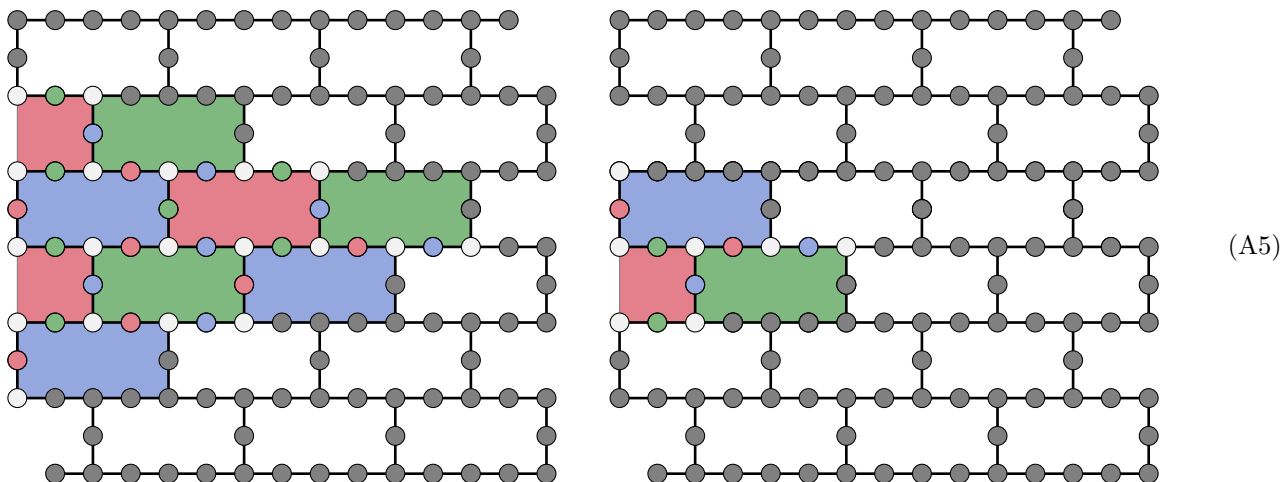
Below, on the left we have green vertical and red horizontal boundaries. On the right we have green vertical and blue horizontal boundaries.



Here the grey qubits are not required to implement the Color Code. We have included an extra corner qubit on both of the above Color Codes for convenience. This corner qubit, and the neighboring qubit, can be moved to nearby unused grey qubits to avoid adding extra physical qubits. Below we focus on the green and red boundary Color Code on the left.

2. Triangle patch

We now consider a triangular patch of the Color Code with a red, green, and blue, boundary. This configuration of the Color Code encodes a single logical qubit that supports transversal S and H gates which generate the full logical Clifford group. This includes the logical XS gate, which has a transversal implementation as described above.



Again, the grey qubits are not required to implement these Color Codes. The smaller patch on the right is equivalent to Steane's code, which has distance three.

Appendix B: Magic state preparation via gauging Clifford measurement on the Color Code

In this appendix, we describe the implementation of a gauging logical measurement of a transversal Clifford operator on the Color Code, which naturally obeys the heavy-hex connectivity constraints.

We introduce a dynamical protocol to fault-tolerantly prepare a logical magic state in the Color Code using qubits laid out on the heavy-hex lattice with nearest neighbor gates and single qubit mid-circuit measurements with global classical communication and feedforward operations. This can be used to prepare encoded magic states by initializing the Color Code in an appropriate logical state, such as $|0\rangle$, and measuring a logical Clifford operator, such as $\sqrt{i}XS^\dagger$. This code deformation creates a non-stabilizer code that is known to support nonabelian D_4 quantum double anyons [33]. Below, we further show that the deformed code is in fact the same as the one studied in Refs. [2, 34, 35]. Interestingly, the non-Clifford logical operation is implemented by switching into and out of the nonabelian topological code and does not require creation or braiding of nonabelian anyons [2].

To measure a transversal logical operator on the heavy-hex lattice we apply the following gauging measurement procedure [22]:

1. Perform single qubit rotations on all vertex qubits to bring the transversal logical operator on each site into the form of an X operator.
2. Initialize all edge qubits in the $|0\rangle$ state.
3. Perform CNOTs from each vertex to all surrounding edges. In each CNOT the vertex is the control qubit and the edge is the target qubit.
4. Measure X on each vertex qubit, and reset to $|\pm\rangle$ conditioned on the measurement outcome.
5. Perform the CNOT circuit from step 3 again.
6. Measure Z on each edge qubit.
7. Apply a Z -type byproduct operator to vertex qubits.
8. Undo the single qubit rotations from step 1.

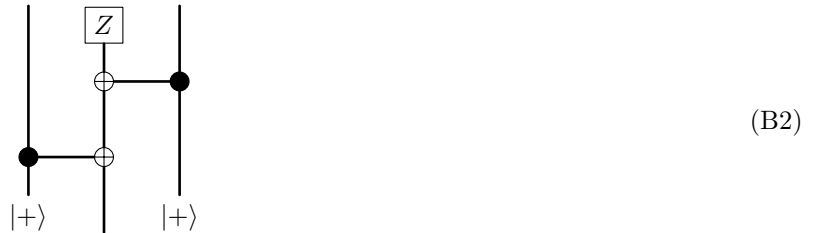
The above procedure measures the global transversal logical operator, but does not measure any other operator that is supported solely on the vertex qubits. The outcome of the logical measurement is recovered by taking the product of all vertex qubit X measurement results. To implement the above procedure scalably and fault tolerantly requires d rounds of quantum error correction for the deformed quantum code that appears between steps 4 and 5, where d is the desired fault distance [22]. Alternatively, fault tolerance can be achieved without scalability by simply repeating the whole gauging measurement procedure as written a sufficient number of times and post-selecting on a consistent measurement outcome or taking a majority vote.

We remark that to perform steps 1 and 8 of the procedure for a Clifford operator requires the application of single site non-Clifford rotations from the third level of the Clifford hierarchy. Steps 2-4 result in the following measurement, shown below for a single vertex.



The qubits initialized in $|0\rangle$ above are edge qubits adjacent a single vertex qubit, which is measured in the X -basis, denoted by the box labeled X . In the full procedure, each internal edge qubit is adjacent to a pair of vertices and consequently it is the target of two CNOT gates. Steps 5-6 result in the following measurement, shown below for a single

edge.



Here, the qubits initialized in $|+\rangle$ correspond to a pair of vertex qubits that are adjacent to an edge qubit which is measured in the Z -basis. More generally the vertex qubits are initialized in $|\pm\rangle$ depending on the outcome of the preceding vertex X measurement in step 4. In the full procedure, each internal vertex qubit is adjacent to three edge qubits, and hence is the control for three CNOT gates. The byproduct operator in step 7 is found by taking a product of Z_v operators on a collection of vertices whose \mathbb{Z}_2 -coboundary (\mathbb{Z}_2 -boundary on the dual lattice) matches the edge measurement results found during step 6, see Ref. [22] for an in depth description.

We now proceed to describe two examples. To provide a high level insight on these examples, we note that when the above gauging measurement procedure is applied to a global symmetry of a topological code, steps 1-4 implement a transformation on the anyon content of the code known as gauging a symmetry. Hence the deformed code that appears after step 4 supports anyons that correspond to gauging the global symmetry on the anyon theory of the initial code. There is a general formalism to calculate the effect that gauging has on a topological state, which depends on how the global symmetry acts on the initial code [36]. Below, we first consider a simple example where the global symmetry is the Color Code's X logical operator, which acts on the anyon content of the theory in a trivial way. The result of gauging this symmetry on the anyon theory is simply to introduce another copy of the surface code. In the second example we consider gauging a global symmetry that permutes the anyon types of the Color Code in a nontrivial way by swapping their X and Y labels [23]. In this case, it is known that gauging such a permutation symmetry on the abelian $\mathbb{Z}_2 \times \mathbb{Z}_2$ anyons of the Color Code leads to a nonabelian D_4 anyon theory [36].

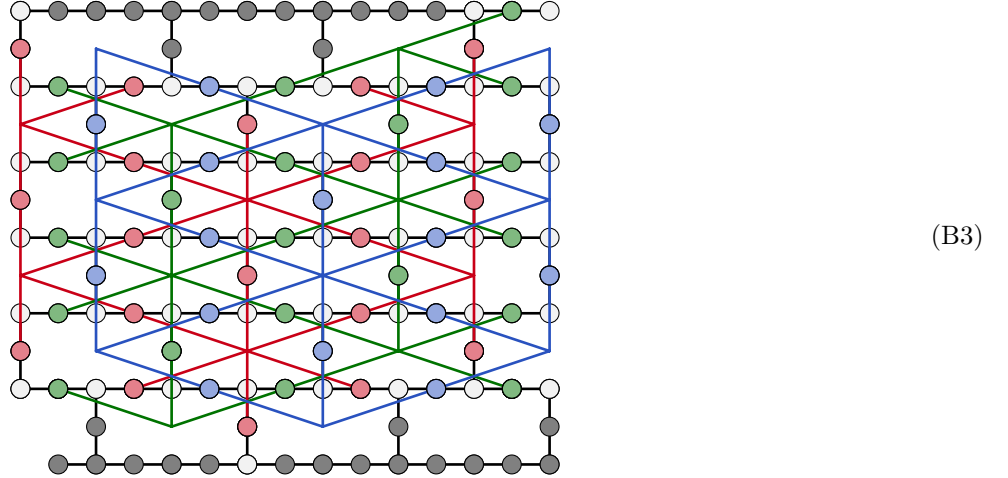
The second half of the gauging measurement procedure, steps 5-7, then correspond to *ungauging* the global symmetry. This is equivalent to condensing the abelian anyons that correspond to gauge charges. In the first example, this simply condenses the e anyons in one copy of the surface code and restores the anyon theory of the Color Code. In the second example, this condenses one of the abelian anyons in the D_4 theory to restore the $\mathbb{Z}_2 \times \mathbb{Z}_2$ anyon theory of the Color Code.

There is a key distinction between our proposal and previous work on preparing nonabelian anyon states on a quantum device [35]. Our procedure demonstrates that by preparing a nonabelian D_4 state on a quantum device we can achieve a useful primitive for universal fault-tolerant quantum computation without the need to manipulate nonabelian anyons directly. This useful primitive is magic state preparation which can be combined with lattice surgery, or transversal, Clifford logic gates to perform universal fault-tolerant quantum computation in two dimensions without requiring the braiding of anyons or defects [2].

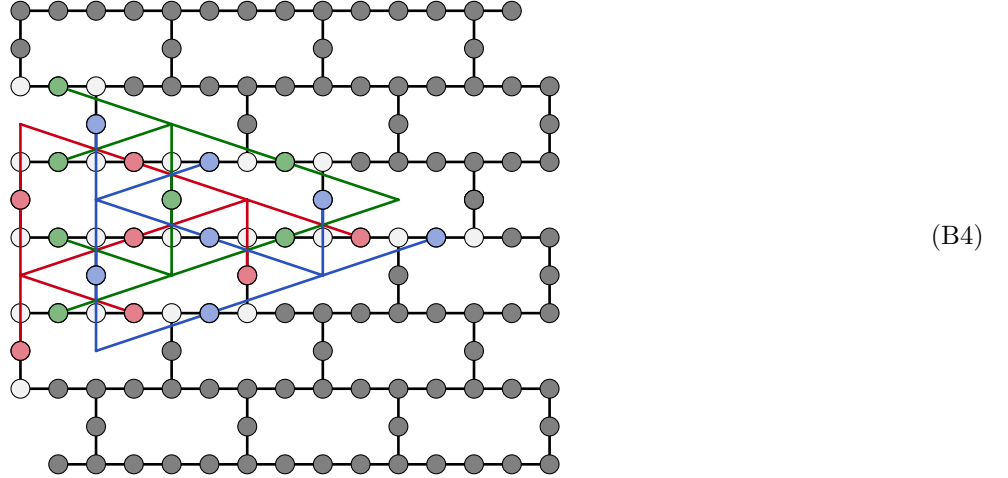
1. Logical X measurement

First, we consider a simple example where no rotation is performed at step 1. In this case the transversal X logical operator is measured directly on the Color Code. Steps 2-4 essentially initializes a new copy of surface code. The resulting deformed code at step 4 is equivalent to three copies of the surface code supported on the red, green, and blue colored

edge sublattices, respectively. This deformed code is shown for the square patch Color Code from Eq. (A4) below.



Similarly, for the triangular patch Color Code in Eq. (A5), measuring the transversal X logical operator leads to a deformed code equivalent to three copies of the surface code with boundary conditions shown below.



Steps 5-7 then measure out the newly initialized surface code, and restore the original Color Code.

2. Logical XS^\dagger measurement

We now discuss applying the gauging measurement procedure to the transversal $\sqrt{-i}XS$, $\sqrt{i}XS^\dagger$, operator on Color Code. For the remainder of this section we do not explicitly write the phase factors that make the XS , XS^\dagger , operators Hermitian. For a square patch of Color Code, see Eq. (A4), this measures a logical CZ gate. Similarly, for a triangle patch of Color Code, see Eq. (A5), this measures a logical XS^\dagger (or XS) gate. By initializing the square or triangle patch Color Codes in the $|++\rangle$ or $|0\rangle$ logical states, respectively, the above measurements produce encoded CZ or T (T^\dagger) magic states.

To perform the gauging measurement on the transversal XS , XS^\dagger , operator we first consider a symmetrized set of stabilizer checks for the code space where each check remains invariant under the symmetry action. In particular, for each plaquette p we have a Z -type check, $\prod_{v \in p} Z_v$, and another check

$$B_p := \frac{1}{2} \left(\prod_{v \in p} X_v \pm \prod_{v \in p} Y_v \right) = \frac{1}{2} (\mathbb{1} + \prod_{v \in p} Z_v) \prod_{v \in p} X_v, \quad (\text{B5})$$

where the (± 1) sign is determined by the parity of up-type vertices in plaquette p . The B_p operator satisfies $B_p^2 = \frac{1}{2} (\mathbb{1} + \prod_{v \in p} Z_v)$ and hence acts as 0 outside the $\prod_{v \in p} Z_v = +1$ subspace, while it acts as $\prod_{v \in p} X_v$ and hence has (± 1) eigenvalues within the $\prod_{v \in p} Z_v = +1$ subspace.

Step 1 of the gauging measurement procedure involves a T rotation on each up-vertex and a T^\dagger rotation on each down-vertex, see Eq. (A3). This leaves the Z -type plaquette checks invariant, and maps the B_p terms to

$$B_p \mapsto B'_p = \frac{1}{2^4} \left(\prod_{v \in p} (X_v - \varepsilon_v Y_v) - \prod_{v \in p} (Y_v + \varepsilon_v X_v) \right) \quad (\text{B6})$$

$$= \frac{1}{2^4} \prod_{v \in p} X_v \left(\prod_{v \in p} (\mathbb{1} - \varepsilon_v i Z_v) + \prod_{v \in p} (\mathbb{1} + \varepsilon_v i Z_v) \right) \quad (\text{B7})$$

$$= \frac{1}{2^3} \prod_{v \in p} X_v \left(\mathbb{1} + \sum_{v < v' \in p} i^{\varepsilon_v + \varepsilon_{v'}} Z_v Z_{v'} + \sum_{v < v' < v'' < v''' \in p} i^{\varepsilon_v + \varepsilon_{v'} + \varepsilon_{v''} + \varepsilon_{v'''}} Z_v Z_{v'} Z_{v''} Z_{v'''} + \prod_{v \in p} Z_v \right) \quad (\text{B8})$$

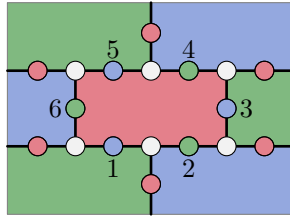
$$= \frac{1}{2^3} \prod_{v \in p} X_v \left(\mathbb{1} + \prod_{v \in p} Z_v \right) \left(\mathbb{1} + \sum_{v, v' \in p} i^{\varepsilon_v + \varepsilon_{v'}} Z_v Z_{v'} \right), \quad (\text{B9})$$

where $\varepsilon_v = +1$ for up type vertices, and $\varepsilon_v = -1$ for down type vertices. In the sums over vertices above we use a vertex ordering starting at the bottom left corner of a plaquette and proceeding counterclockwise. The operator above is written for a hexagonal plaquette with six vertices, for a boundary plaquette with four vertices we instead have

$$B'_p = \frac{1}{2^2} \prod_{v \in p} X_v \left(\mathbb{1} + \sum_{v, v' \in p} i^{\varepsilon_v + \varepsilon_{v'}} Z_v Z_{v'} + \prod_{v \in p} Z_v \right). \quad (\text{B10})$$

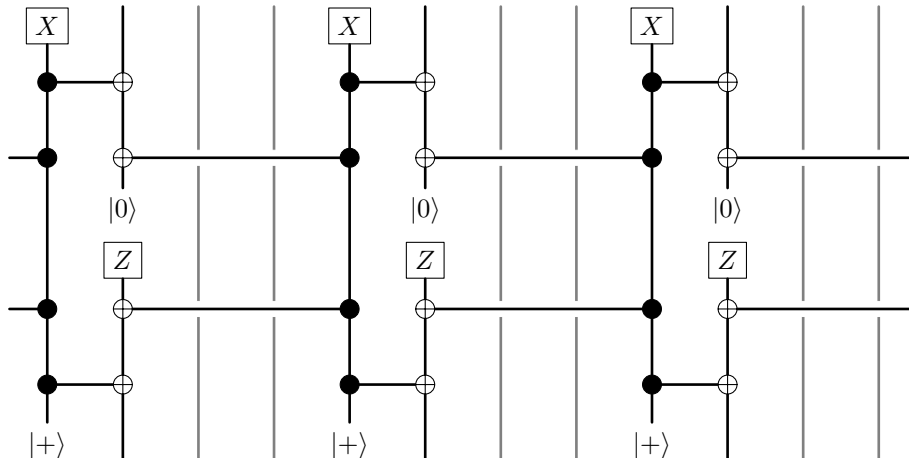
After step 4 of the gauging measurement procedure the code has been deformed into a new code supported on the edge qubits. While the outcomes of the X_v measurements at step 4 are random, we can apply a byproduct operator to arrive at the deformed code corresponding to all $X_v = +1$ outcomes. The byproduct operator is a product of Z string operators on edges that end on the $X_v = -1$ outcome vertices and on open boundaries. For simplicity we focus on the $X_v = +1$ outcome deformed code.

The deformed code is stabilized by three plaquette checks per bulk plaquette, and two per boundary plaquette. Two of the bulk plaquette checks are Z -type, and take the form $Z_1 Z_3 Z_5, Z_2 Z_4 Z_6$, using the numbering convention for the edges around a plaquette shown below. These Z -type plaquettes originate from deformed Z -type plaquette checks in the Color Code, combined with additional stabilizer checks that are introduced on the edge qubits initialized in $|0\rangle$.



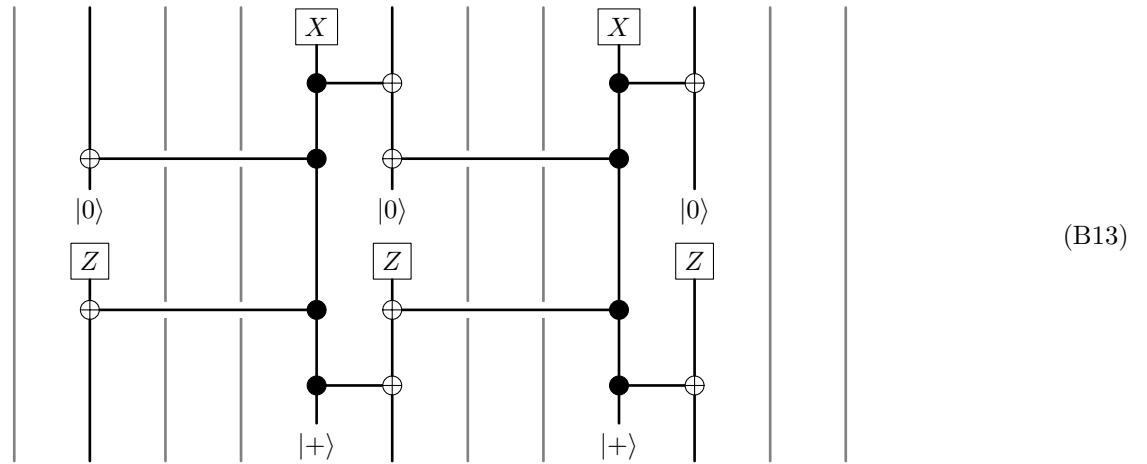
(B11)

The Z plaquette checks are products of Z operators on edges of a single color in the boundary of the plaquette. A circuit to measure the $Z_1 Z_3 Z_5$ check is shown below, where the vertex and edge qubits in the boundary of the plaquette are ordered starting from the vertex qubit in the bottom right corner, and proceeding counterclockwise.

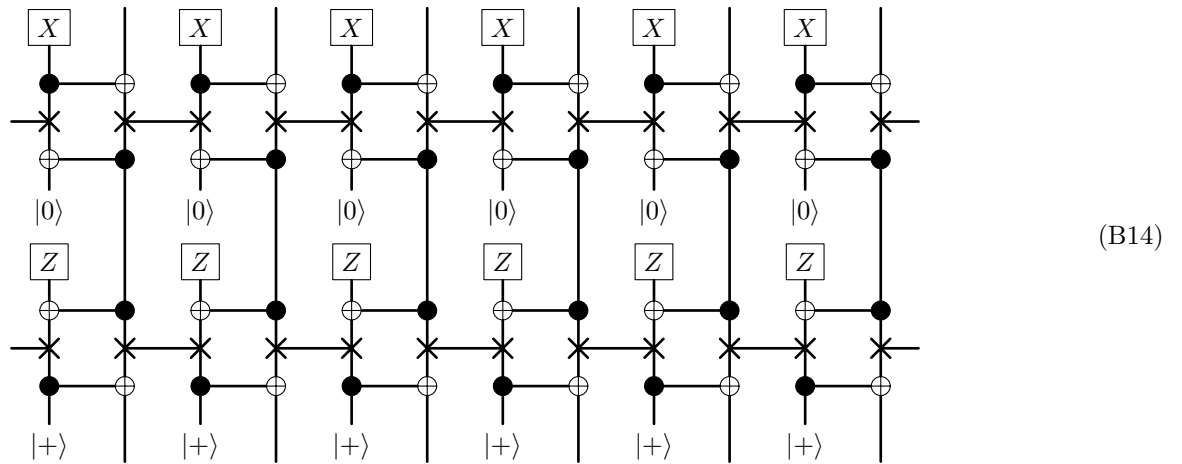


(B12)

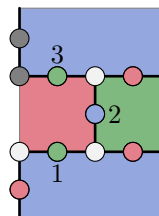
An alternative circuit with fewer measurements can also be used.



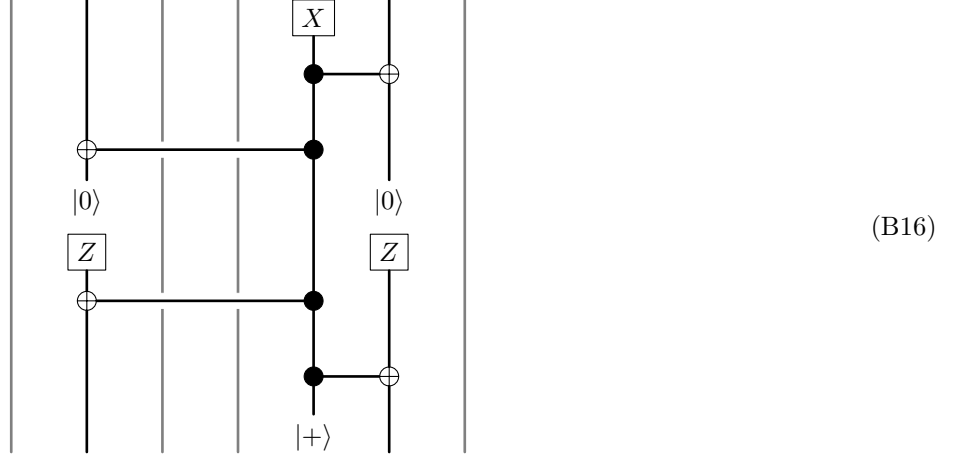
Here, the long range CNOT gates must be mediated by swaps or bridge qubits [37]. Similar circuits can be used to measure $Z_2Z_4Z_6$. The circuit in Eq. (B12) for both Z -type plaquette checks can be implemented simultaneously using swaps as follows.



A similar approach applies to simultaneously implement the circuit in Eq. (B13) for both Z -type plaquette checks. Boundary plaquettes have three edges, which are numbered similar to the convention above.



The boundary Z_1Z_3 check can be measured similar to above via the following circuit.



(B16)

In the Z -type check measurement circuits above we have reinitialized all physical qubits in the $|0\rangle$ state. This is to ensure that the post-measurement state lies in the $(+1)$ -eigenspace of all Z -type plaquette checks, which is required to gain useful information from a subsequent measurement of the \tilde{B}_p check.

The remaining plaquette check is derived by deforming the symmetrized plaquette check in the Color Code, see Eq. (B8),

$$\begin{aligned} \tilde{B}_p &= \frac{1}{2^4} \prod_{e \perp p} X_e (\mathbb{1} + \prod_{e \in p} Z_e) \\ &\quad \left(\mathbb{1} + \sum_{v < v' \in p} i^{\epsilon_v + \epsilon_{v'}} Z_{\langle v, v' \rangle} + \sum_{v < v' < v'' < v''' \in p} i^{\epsilon_v + \epsilon_{v'} + \epsilon_{v''} + \epsilon_{v'''}} Z_{\langle v, v' \rangle} Z_{\langle v'', v''' \rangle} + Z_1 Z_3 Z_5 \right), \end{aligned} \quad (\text{B17})$$

where the notation $e \perp p$ denotes the edges that meet the boundary of plaquette p at a single vertex, in Eq. (B11) these are the red edges. The notation $\langle v, v' \rangle$ denotes the counterclockwise path from v to v' in the boundary of plaquette p , and $Z_{\langle v, v' \rangle} = \prod_{e \in \langle v, v' \rangle} Z_e$. For the term $Z_1 Z_3 Z_5$ we have used the edge numbering from Eq. (B11). We remark that no Z_6 terms appear in the sum of Z terms in the second line of Eq. (B17), as they are factored out in the $(\mathbb{1} + \prod_{e \in p} Z_e)$ term. We note that $(\mathbb{1} + Z_1 Z_3 Z_5)$ can be further factored out from the sum of Z terms in the second line of Eq. (B17), which follows from deforming the $(\mathbb{1} + \prod_{v \in p} Z_v)$ term that is factored out in Eq. (B9). We then have

$$\begin{aligned} \tilde{B}_p &= \frac{1}{2^4} \prod_{e \perp p} X_e (\mathbb{1} + Z_1 Z_3 Z_5) (\mathbb{1} + Z_2 Z_4 Z_6) (\mathbb{1} + Z_1 + Z_2 - Z_1 Z_2 + Z_4 + Z_5 - Z_4 Z_5 + Z_1 Z_4 \\ &\quad + Z_1 Z_5 - Z_1 Z_4 Z_5 + Z_2 Z_4 + Z_2 Z_5 - Z_2 Z_4 Z_5 - Z_1 Z_2 Z_4 - Z_1 Z_2 Z_5 + Z_1 Z_2 Z_4 Z_5) \end{aligned} \quad (\text{B18})$$

$$= \prod_{e \perp p} X_e \frac{1}{2} (\mathbb{1} + Z_1 Z_3 Z_5) \frac{1}{2} (\mathbb{1} + Z_2 Z_4 Z_6) CZ_{12} CZ_{45}, \quad (\text{B19})$$

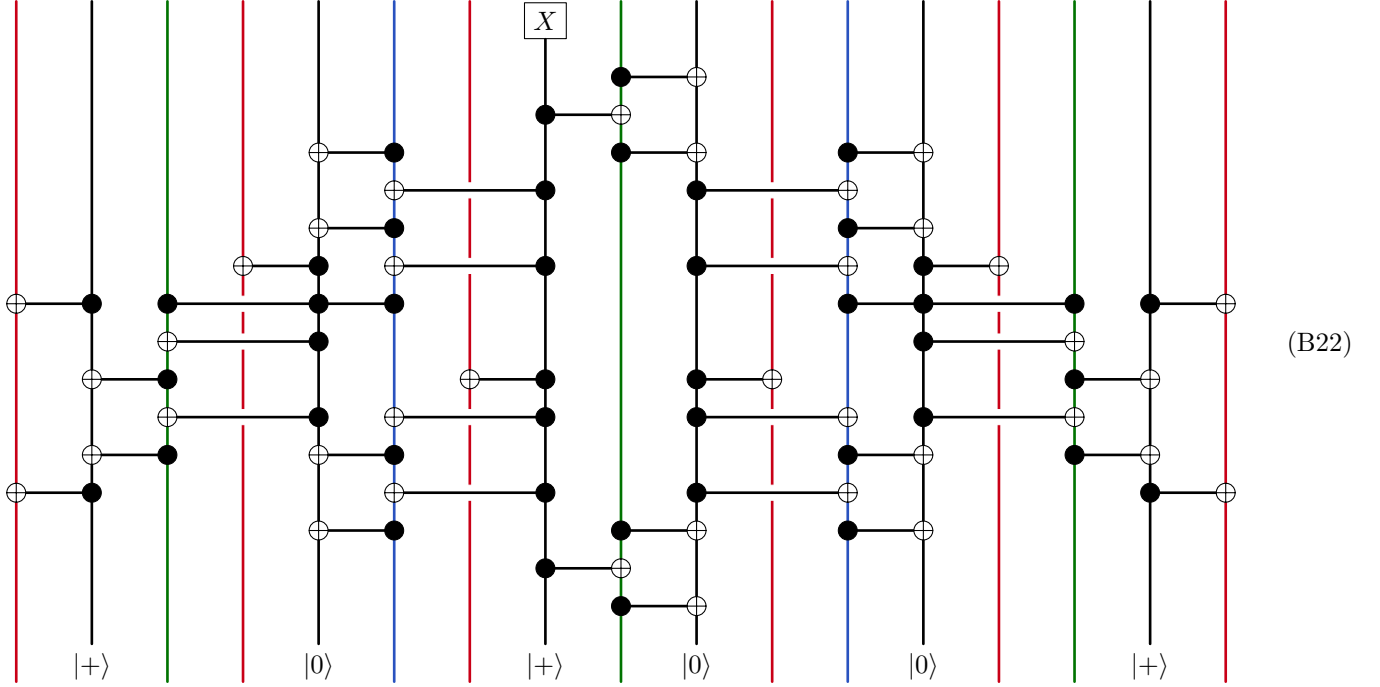
where we have used the factoring out of the $Z_1 Z_3 Z_5$ and $Z_2 Z_4 Z_6$ terms to ensure that Z_3 and Z_6 do not appear in the additional sum over Z terms in the first equation. We have used that $CZ_{12} = \frac{1}{2}(\mathbb{1} + Z_1 + Z_2 - Z_1 Z_2)$ in the second equation. We remark that \tilde{B}_p can be written in a more symmetric fashion as

$$\tilde{B}_p = \prod_{e \perp p} X_e \frac{1}{2} (\mathbb{1} + Z_1 Z_3 Z_5) \frac{1}{2} (\mathbb{1} + Z_2 Z_4 Z_6) CZ_{12} CZ_{23} CZ_{34} CZ_{45} CZ_{56} CZ_{16}, \quad (\text{B20})$$

using the fact that $CZ_{23} CZ_{34} CZ_{56} CZ_{16}$ acts trivially in the $Z_1 Z_3 Z_5 = +1, Z_2 Z_4 Z_6 = +1$, subspace. This demonstrates that the choice of starting point in the numbering of edge qubits involved in \tilde{B}_p is arbitrary. To measure \tilde{B}_p we can first measure $Z_1 Z_3 Z_5, Z_2 Z_4 Z_6$, and apply a correction to ensure we are in the $Z_1 Z_3 Z_5 = +1, Z_2 Z_4 Z_6 = +1$, subspace and then measure the simpler operator

$$\tilde{B}'_p = \prod_{e \perp p} X_e CZ_{12} CZ_{45}. \quad (\text{B21})$$

This approach means that the measured value of \tilde{B}'_p is only useful for inferring the measured value of \tilde{B}_p when we can ensure the measured values of the Z -type plaquette operators are $Z_1 Z_3 Z_5 = +1, Z_2 Z_4 Z_6 = +1$. This feature requires special care when decoding, and can be handled by a just-in-time or on-the-fly decoder [2, 38–40]. A circuit on the heavy-hex lattice to measure \tilde{B}'_p is shown below.



In the above we use the ordering of qubits following the numbering below.



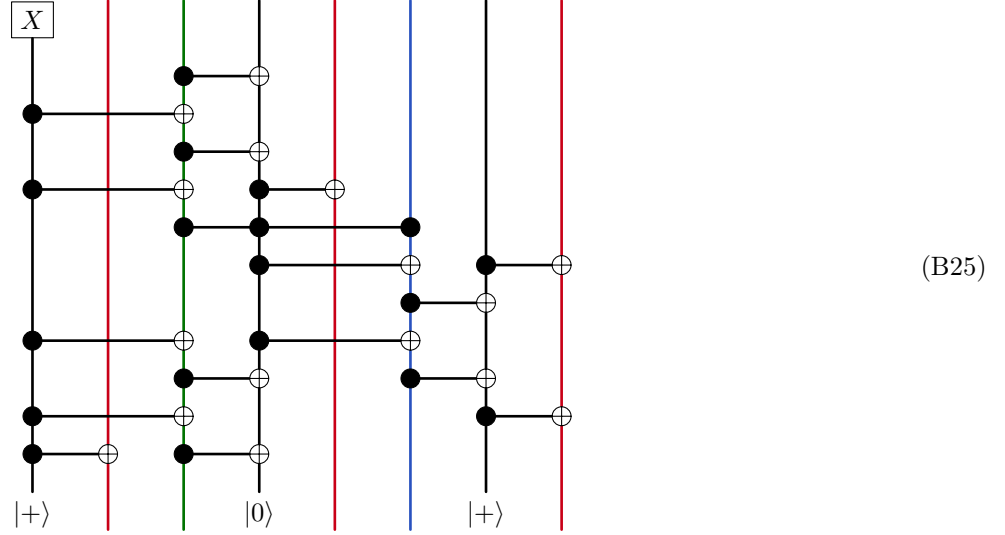
In the circuit above the unmeasured $|0\rangle$ and $|+\rangle$ states are required to be in the specified state to measure the desired \tilde{B}'_p operator. These states can be measured in the appropriate basis to provide additional flag information to detect errors. An alternative circuit with fewer CNOT gates can be found by removing the final two CNOT gates between qubits 8 and 9 and measuring qubit 9 in the X basis, in this case the measurement result is the product of the X measurement results on qubits 7 and 9.

Similar to the bulk deformed plaquette operator, the deformed boundary plaquette check can be written

$$\tilde{B}_p = \prod_{e \perp p} X_e \frac{1}{2} (1 + Z_1 Z_3) CZ_{12}, \quad (\text{B24})$$

where the number of edges that meet the boundary plaquette at a single vertex can be two, three, or four, depending on the boundary condition. Similar to above, in the $Z_1 Z_3 = +1$ subspace we can measure the simpler operator $\tilde{B}'_p =$

$\prod_{e \perp p} X_e CZ_{12}$. A circuit to implement this measurement on the heavy-hex lattice is shown below.



Above, the qubits are ordered as follows.



In the appendices of Ref. [33] the deformed code described above, up to a change of basis on individual qubits, was demonstrated to be equivalent to the nonabelian D_4 quantum double anyon theory. Here, we have further shown that the deformed code is in fact the same as the one studied in Refs. [2, 34, 35], up to a codespace-preserving redefinition of the checks.

The smallest nontrivial example of the XS measurement can be performed on a distance three triangle patch of Color Code, shown embedded into the heavy-hex lattice in Eq. (A5). In this case the deformed code is defined on the edges of the patch shown below.



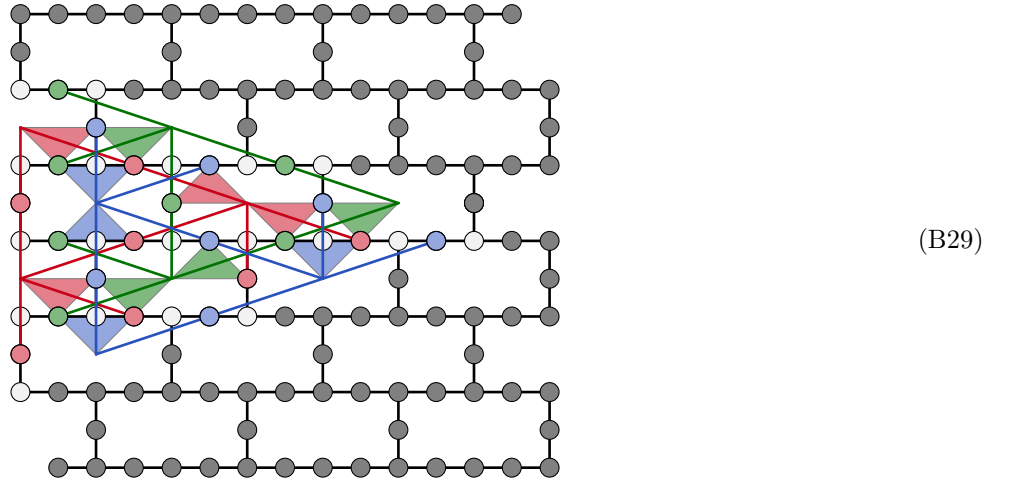
In this case the stabilizer group of the deformed code commutes as it is generated by the checks

$$\langle Z_1 Z_4, Z_2 Z_5, Z_3 Z_6, X_1 X_4 CZ_{23}, X_2 X_5 CZ_{13}, X_3 X_6 CZ_{12} \rangle, \quad (\text{B28})$$

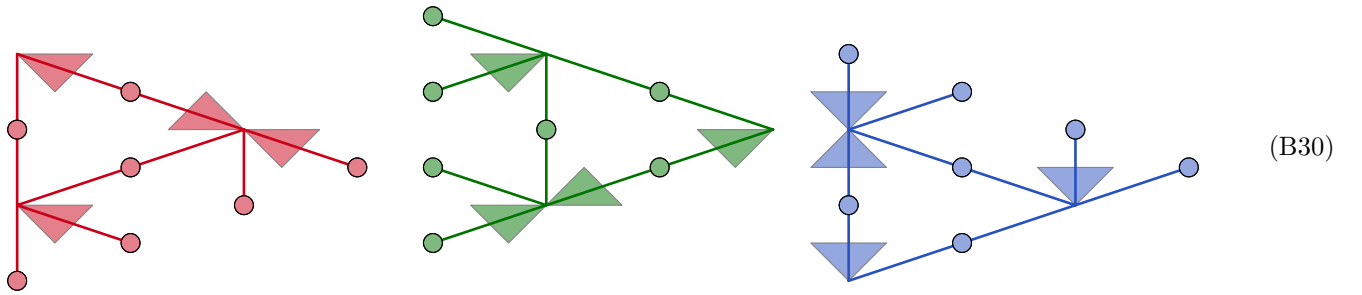
where we have used the numbering convention in Eq. (B27). This code is equivalent to three Bell pairs on qubits 14, 25, 36, that have been entangled via a CCZ gate on qubits 123. This code can only detect errors due to a reduction to the Color Code distance induced by the code deformation. However, the correction chosen to return to the code space does not matter for the XS logical measurement in this example, and on larger triangle patches, as the code space contains only the desired logical magic state.

A larger example of the XS measurement can also be implemented on heavy-hex using the embedding a distance five triangular Color Code shown on the left of Eq. (A5). This results in a deformed code that is similar to three copies of the surface code on the lattices shown below, in that it has the same Z -type plaquette terms. However the X -type star

terms in the deformed code involve additional CZ operators, which are indicated via colored triangles that connect each vertex to pairs of edge qubits below.



The three sublattices that appear are depicted separately below, for clarity.



Appendix C: Gauging logical measurement proof

In this appendix, we prove that the gauging logical measurement scheme of Ref. [22] works without assuming that the logical operator is a Pauli product. Let us take a logical operator of the product form $C_L = \prod_i U_i$, where $U_i = U_i^{-1}$ and i runs over the data qubits. Further, let us define an ancilla system where each ancilla is connected to a small subset of data qubits. If every ancilla is connected to a pair of qubits, one can define gauge operators for every data qubit

$$A_i = U_i \prod_{a \in \partial i} X_a. \quad (\text{C1})$$

The product of these operators is the logical operator C_L we aim to measure. The claim is that one can measure these gauge operators and (i) the product of measurements $\sigma_L = \prod_i m_i$ is the logical eigenvalue and (ii) the measurement outcome of the ancilla qubits will be sufficient to restore the correct post-measurement state $(1 + \sigma_L C_L) |\psi\rangle_Q$.

Taking an arbitrary code state, and initializing the ancillas in the $|0\rangle$ state upon measuring the gauge operators individually we get

$$\prod_{Q' \subset Q, |Q'| \leq \frac{|Q|}{2}} \left(\prod_{i \in Q'} m_i U_i + \prod_{i \in Q/Q'} m_i U_i \right) |\psi\rangle_Q \otimes |v_{Q'}\rangle_A, \quad (\text{C2})$$

where m_i are the measurement outcome of gauge A_i , the summation goes through every Q' subset of data qubits, and $|v_{Q'}\rangle_A$ is a product state on the ancillas where each ancilla is $|0\rangle$ ($|1\rangle$) if it is connected to an even (odd) number of data qubits in Q' . Exploiting that $U_i = U_i^{-1}$ we can rewrite the equation above as

$$(1 + \sigma C_L) \prod_{Q' \subset Q, |Q'| \leq \frac{|Q|}{2}} \prod_{i \in Q'} m_i U_i |\psi\rangle_Q \otimes |v_{Q'}\rangle_A. \quad (\text{C3})$$

Once the ancillas are measured in a certain state $|v_{Q'}\rangle_A$ the state (up to a global phase) becomes

$$(1 + \sigma C_L) \prod_{i \in Q'} U_i |\psi\rangle_Q, \quad (\text{C4})$$

and the correct post-measurement state can be restored if the measured state $|v_{Q'}\rangle_A$ determines the subset Q' modulo Q .

The strategy for constructing a suitable ancilla graph and determining the correction operator from the measurement can be found in the main text.

Appendix D: Pipelining the gauging measurement circuit

In order to reduce the number of idling operations in the circuit, each of which comes with a single-qubit depolarizing channel, we performed some circuit optimizations that preserve the effective CX ordering of the superdense circuit and the flagging of the gauging measurement. Fig. 5 shows the circuits from the main text as well as the pipelined version where we allow measurements to be performed at the same timestep as CX gates.



Figure 5. (a) The same circuit as in the main text. (b) Pipelined circuit with 18 CX time steps and 3 measurement/reset time steps.

Appendix E: Transitioning to a matchable code

Fig. 6 shows a circuit that converts the grafted surface code into a regular surface code. Since the second reset-CX-measurement stage only acts on the boundaries of the code, we suspect that more efficient conversion circuits exist. Perhaps ones with a single reset-CX-measurement stage.

The last round of the transformation (not shown) is a regular surface code stabilizer measurement cycle, where the appropriate products of measurement outcomes (involving at most two) are included in the corresponding detectors of the last step shown in Fig. 6. These deformation circuits were found using *crumble* [27].

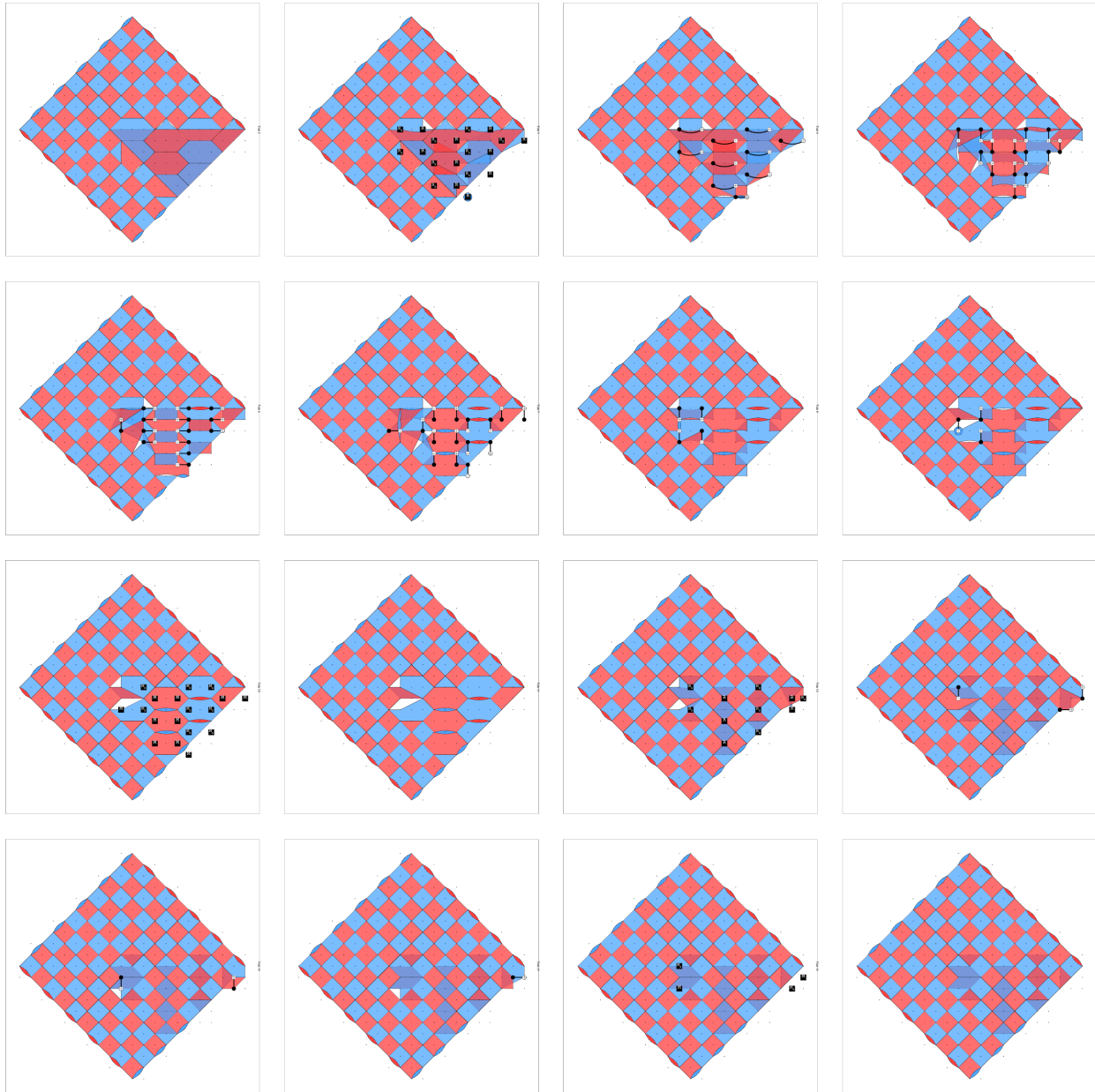


Figure 6. The full circuit for the transition of the grafted surface code to a regular (rotated) surface code. These steps cover the first three diagrams in Fig. 4(c).